2021

A Case Study: Influence of Circuit Impedance on the Performance of Class-E² Resonant Power Converter for Capacitive Wireless Power Transfer

Yashwanth Bezawada
Old Dominion University, ybeza001@odu.edu

Yucheng Zhang
Old Dominion University, yzhang@odu.edu

A Case Study: Influence of Circuit Impedance on the Performance of Class-E^2 Resonant Power Converter for Capacitive Wireless Power Transfer

Yashwanth Bezawada and Yucheng Zhang *

Electrical and Computer Engineering, Old Dominion University, Norfolk, VA 23529, USA; ybeza001@odu.edu
* Correspondence: yzhang@odu.edu; Tel.: +1-757-683-5483

Abstract: The evolution of power electronics led to rapid development in wireless charging technology; as a result, a single active switch topology was introduced. The present market utilizes inductive wireless power transfer (IPT); because of the disadvantages of cost, size, and safety concerns, research on wireless power transfer was diverted towards capacitive wireless power transfer (CPT). This paper studies the optimal impedance tracking of the capacitive wireless power transfer system for maximum power transfer. Compared to prior methods developed for maximum power point tracking in power control, this paper proposes a new approach by means of finding impedance characteristics of the CPT system for a certain range of frequencies. Considering the drone battery as an application, a single active switch Class-E^2 resonant converter with circular coupling plates is utilized. Impedance characteristics are identified with the help of equations related to the input and resonant impedance. The impedance tracking is laid out for various resonant inductors, and the difference in current peak is observed for each case. Simulations verify and provide additional information on the reactive type. Additionally, hardware tests provide the variation of input current and output voltage for a range of frequencies from 70 kHz to 300 kHz. Efficiency at the optimal impedance points for a resonant inductor with 50 μH and 100 μH are tested and analyzed. It is noted that the efficiency for a resonant inductor with 50 μH is 8% higher compared to the CPT with a 100 μH resonant inductor. Further hardware tests were performed to investigate the impact of frequency and duty cycle variation. Zero-voltage-switching (ZVS) limits have been discussed with respect to both frequency and duty cycle.

Keywords: capacitive wireless power transfer system (CPT); Class-E^2 resonant converter; Zero-voltage-switching (ZVS); optimal impedance tracking

1. Introduction

Recent developments in power electronics in reference to switching devices have made an impact in the field of wireless power charging, which has evolved its concept from low power to high power applications because of its safe, reliable, and convenient charging techniques. Especially, after the success of wireless mobile charging in the present market, the topics related to wireless power transfer (WPT) have expanded to medical [1–3], automobile [4–7], and automation areas [8–13]. In the past decade, inductive wireless power transfer (IPT) and resonant wireless power transfer have drawn tremendous attention in both industry and academic fields. Inductive power transfer (IPT) utilizes loosely coupled inductive coils as a transmitter and a receiver to transfer power in the form of magnetic fields. IPT can transfer power over a 100 cm range with high efficiency [14,15] but it requires bulk and expensive ferrite cores instead of coils [1]. This has been a drawback of the existing WPT systems [8]. As an alternative, capacitive wireless power transfer (CPT) has shown promising results, as shown in Figure 1. CPT utilizes an electric field as a medium to transfer power, also known as capacitive coupling interface. Capacitive films are a better substitute for bulky and expensive ferrite cores. Additionally, capacitive coupled

WPT systems can eliminate eddy current losses and concerns related to the temperature of the metal.
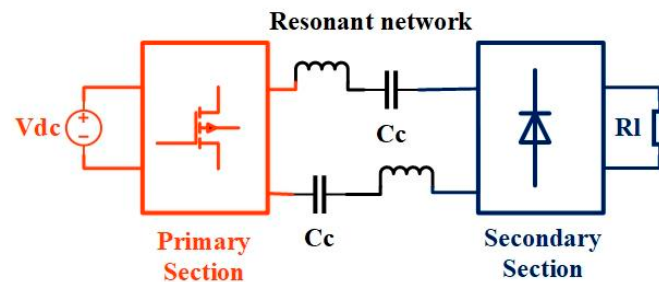

Figure 1. CPT block with resonant network.

1.1. Review of Capacitive Coupling Structures

From the application point of view, capacitive films provide flexibility when designing the coupling section. Capacitive coupling utilizes multiple plates to generate electric fields. Based on the coupling interface, different structures such as 2-plate, 4-plate, and 6-plate were designed to improve the coupling capacitance for maximum power transfer [16,17]. Coupling plates with high air gaps result in low capacitance (typically in tens of pF) [18]. In such cases, the addition of a compensation network can be more effective. CPT is the foremost coupling method to apply for high power applications with a transmission range of less than 10 cm. For these cases, the CPT system can achieve an efficiency of over 93% [19]. Unlike inductive coils that generate magnetic fields around its core, coupling plates tend to contain electric fields within the coupling section area. In order to achieve effective capacitive coupling, the medium is considered dielectric with a transfer distance of 1 mm [19–23]. This increases the coupling capacitance and ultimately overcomes the requirement of high voltage to the coupling section. Additionally, it minimizes the number of electromagnetic components (bulk inductors) in the design of resonant networks, which leads to a reduction in EMI. Considering that the coupling plates are closer to each other, this also overcomes the safety concerns related to electromagnetic fields. Mutual capacitance is one of the factors that influence the voltage gain at the resonant network. For closely capacitive coupled sections, the cross-coupling capacitance C_M (also known as mutual capacitance) will be low in comparison to coupling capacitance.

1.2. Introduction of Power Topologies for CPT

The system is designed considering the drone battery as an application, with a rating of 100 W and a transfer distance within a 1 cm range. For near field application, the capacitive wireless power transfer method has proven efficient and safe [24]. Inverter and rectifier topologies are key to the WPT system. The inverter function is to provide AC voltage to the coupling section but it has a crucial role in enhancing efficiency. For CPT, various inverter and rectifier circuits are utilized for power conversion (DC-AC or AC-DC). Based on the inverter section, the topologies are classified into resonant and non-resonant converters. Non-resonant converters can be realized by high-frequency power amplifiers such as Class-D, Class-E, Class-EF, and Class-ø [25] or full-bridge/half-bridge circuits. The full-bridge and half-bridge converters are commonly used for high power applications like electric vehicle charging [26] or high voltage applications like plasma treatment in the medical field [2]. The advantages of power amplifier-based topology include the increase in transfer distance [27–29]. The resonant topologies consist of pulse width modulation (PWM) converters. Advantages include that they are simple circuits, non-sensitive to the variation of circuit parameters, and the system efficiency is high for large coupling capacitances. For the PWM converter, if the parameters are large enough to maintain a continuous current working mode, these variations do not impact the system power. Resonant converters include single-switch topologies such as Buck-Boost, Cuk, Sepic, and Zeta converters that realize CPT systems [30]. They were developed to minimize

the number of semiconductor devices that lead to a reduction in semiconductor losses. But it adds voltage stress to the single switch that potentially could be damaged, especially considering ZVS for high power applications, which will be discussed further in the paper.

*1.3. Discussion on Parameter Variation and Maximum Power Transfer*

For long-distance, loosely coupled CPT systems, the mutual capacitance is limited. In such cases, it requires increasing the plate voltage for sufficient power transfer [31]. To achieve efficient power transfer both IPT and CPT systems require a compensation network. This is designed to resonate with the coupling section, and the system is operated close to the resonant frequency. The addition of an LC network improves the overall performance of the system, as it not only eliminates the reactive power but also amplifies the AC signal to the coupling section. Misalignment is one of the key issues in WPT that has an impact on the overall impedance of the system by adding the reactance to the circuit, which can be eliminated by tuning the switching frequency. Several works have noticed the influence on power factor and the impedance characteristics with the variation in load resistance, coupling capacitance, and the addition of external capacitor. Reference [32] has proposed a bi-lateral LC-compensation network. It can be noted that the power factor varies from 0.902 to 0.977 when the load resistance changes from 30.2 Ω to 70.8 Ω and coupling capacitance from 310 pF to 1490 pF, respectively. The optimal load of the double-sided LC-compensated CPT is analyzed in [33]. The optimal load solely improves the AC-AC efficiency of the resonant network, DC-DC efficiency was only 78.4% with 109.3 W output power. To quantify the connection between the optimal load and external capacitance, the impedance characteristics of the full-bridge inverter and rectifier are presented in [34]. To improve the efficiency, a parameter design method is proposed which limits the external capacitor to ensure that the voltage stress is in a reasonable range. Recent works [35] include power transfer tracking for a range of load variations from 5 Ω to 1 kΩ, the maximum efficiency for 10 W is found to be 70%.

In addition to the previous works, this paper focuses on optimal impedance tracking. It presents the circuit's behavior for a range of frequencies. This method can identify the maximum power transfer tracking points for a range of frequencies. Impedance tracking is performed for various resonant inductors. The gain, bandwidth, and efficiency were observed for each resonant inductor. Additionally, the impact of the duty cycle on the CPT system were noted. Section 2 consists of a mathematical model and analysis of the Class-E^2 converter. Several equations were considered for parameter calculation, and the frequency limits for achieving ZVS property were determined. Section 3 consists of theoretical analysis; equations are derived considering the equivalent circuit of the receiving section. Plots are presented based on the equations and simulations. Further, the circuit was verified experimentally for two cases. The analysis includes the record of change in input current, switching current, and resonant network current with respect to the frequency. The maximum power transfer points were measured for both cases with the help of hardware tests. The final section includes a discussion on ZVS limits. The ZVS property is discussed for various frequencies and the duty cycle values and the plot is presented for early, exact, and late ZVS.

2. Theoretical Analysis of Class-E^2 Capacitive Wireless Power Transfer System

This section presents the mathematical model of the CPT system. For high-frequency power circuits, power losses of semiconductor components make a significant contribution to the system's efficiency. With the advancement in MOSFET technology, the operational limits of devices have expanded. This expansion has led to the use of single-active switch topologies for high-power WPT systems. Single-active switch topologies are introduced in [36], these topologies can handle power up to 1~3 kW. With minimal circuitry, these topologies are cost-effective, reliable, efficient, and easy to control. In [36], prior to Class-E^2, a modified buck–boost converter known as a switch-inductor-inductor-diode (SLLD) has provided legitimate results. This has sensitivity issues because of the cable's length and

adds low inductance to the resonant network, which leads to the requirement for a high switching frequency. Compared to buck–boost, Class-E^2 has shown better performance as it eliminates the noises with the addition of a resonant network. Class-E^2 converter is shown in Figure 2; it is the combination of Class-E inverter and Class-E rectifier. It consists of a simple LC resonant network to enhance the power transfer. Analysis of the Class-E^2 converter can be divided into three sections: Class-E inverter, resonant network with coupling capacitors, and Class-E rectifier.
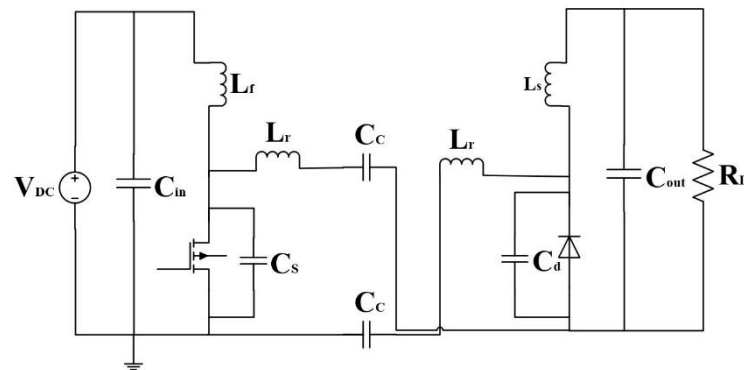
Figure 2. Class-E^2 converter with compensation network.

2.1. Class-E inverter and It's ZVS Limits

The input section consists of a single active switch class-E inverter that functions as a DC-AC voltage converter. Shunt capacitance connected across the switch achieves the ZVS property. Frequency is one of the key factors for calculation of the shunt capacitors, a variation of frequency will impact the ZVS property based on the limits of the capacitor. When the operating frequency is higher than the resonant frequency, the ZVS property remains, to an extent. But the capacitor starts discharging below a resonant frequency, resulting in the loss of ZVS property. For high frequencies, i.e., over a certain frequency, the ZVS condition is lost. In this case, a variation of the duty cycle could help to regain the ZVS but, with a low duty cycle, voltage spikes are noticed at MOSFET, increasing conduction losses. Variation of the duty cycle is critical and will be examined in the discussion section. The choke inductor is connected in series at the input section to handle the sudden changes in current. As DC current flows through the choke inductor L_f, it acts as a short circuit and the DC link will behave as an open circuit. Selection of the choke inductor is crucial: it can resonate with the shunt capacitor, resulting in a second resonant point. The impact of shunt capacitance on the resonant point is recorded. To operate class-E inverter in ZVS condition, the frequency limits are presented based on the impedance region (i.e., inductive/capacitive) of the resonant network. Here, the resonant network needs to be inductive to achieve ZVS [37–40]. This requires the circuit to be operated at frequencies higher than f_1. When the equivalent impedance of the resonant network with shunt capacitance goes to capacitive region, Class-E inverter loses ZVS property for frequencies over f_2. f_1 and f_2 are the lower and upper frequency limits to achieve ZVS condition, which are calculated using (1) and (2)

$$f_1 = \frac{1}{2\pi\sqrt{2 \times L_r C_1}} \tag{1}$$

$$C_1 = \frac{\left(\frac{C_c}{2}\right) \times C_i}{\frac{C_c}{2} + C_i} \qquad f_2 = \frac{1}{2\pi\sqrt{2 \times L_r C_{eq}}} \tag{2}$$

$$C_{eq} = \frac{C_s C_1}{C_1 + C_s} \tag{3}$$

The operating frequency should be within $[f_1, f_2]$ to achieve ZVS. Equations (1)–(3) concludes $f_1 < f_2$. C_i and R_i are the series capacitance and resistance of the rectifier section; further explanation on C_i and R_i is provided in Figure 4 later in this section. The impedance of both the resonant network and the rectifier section influences ZVS condition and the current through MOSFET. Parameters of the Class-E inverter are calculated by using (4) and (5).

The minimum choke inductance is calculated by using

$$L_f = 2\left(\frac{\pi^2}{4} + 1\right)\frac{R_i}{f}$$

(4)

The reactance of the shunt capacitor is calculated by using

$$Z_{C_s} = \frac{1}{\omega C_s} = 0.54466 R_i$$

(5)

2.2. Coupling Section with Resonant Network

Resonant network is the critical part of the CPT system, it influences the power delivered to the rectifier. Achieving resonant point is one of the objectives of the CPT design. Shunt capacitance connected across the diode (C_i) and switch (C_s) have a minimal impact on the resonant point. The shape of the coupling plates is selected based on the application; it determines the power transfer ability of the CPT system. For this paper, circular plates with the vertical structure are realized. From [37], circular plates have shown better performance over square plates by minimizing the edge effect. Additionally, square plates are vulnerable to circular displacement. Figure 3a presents the setup of the coupling plate pair. Here, the medium is considered as dielectric resulting in high coupling capacitance. Figure 3b presents the front and back side of the coupling capacitor; these two plates are placed on top of each other. Overall, four plates are utilized to form two pairs as a capacitive coupling interface. The diameter of the plates is 5 cm with a thickness of 1 mm. A copper foil is used as an electrode, and piezoelectric (PZT is also known as lead zirconium titanate) is used as a dielectric. Because of a high dielectric value with a 2 mm distance, coupling capacitance is measured as 40 nF. For the presented coupling structure, the primary and secondary side coupling capacitance ($C_C - C_M) \approx C_C$. Here, the coupling capacitance is high enough to ignore the mutual capacitance between the plate pairs. High coupling capacitance allows the Class-E^2 converter to operate at a resonant frequency of 111 kHz. Additionally, low-value inductors can be considered for the design of a resonant network.

(a) (b)
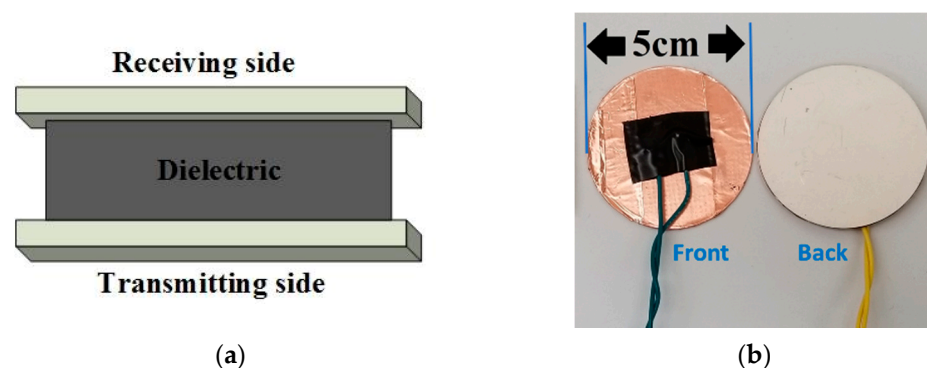
Figure 3. Circular capacitive-coupling plates manufactured for hardware tests in lab.

2.3. Class-E rectifier and its Equivalent Circuit

The rectifier circuit consists of a single active diode connected to a shunt capacitor for achieving ZVS on the receiving section. The low pass LC filter is connected at the output

end to eliminate AC signals to the load. The values of the LC circuit are dependent on the load resistance presented in (6) and (7) i.e., (2) and (3) from [41].

The inductance of the resonant inductor is calculated by

$$L_r = \frac{1}{4\pi^2 f^2 C_c} \tag{6}$$

The shunt capacitance of the diode for 0.5 duty cycle is

$$C_d = \frac{1}{\pi \omega R_L} \tag{7}$$

One of the key points to consider is that, with the additional compensation circuitry, the resonant point is also dependent on the other parts of the circuit such as the rectifier and the switch. To be precise, the resonant point depends on the shunt capacitor connected across the diode. To perform analysis, the Class-E rectifier is modified into an equivalent circuit as shown in Figure 4. As the choke inductor (L_S) acts as a short circuit and the output capacitor (C_{out}) acts as an open circuit, they are ignored for the resonant section. For analysis purposes, Class-E rectifier is modified into its equivalent circuit. Load resistance and shunt capacitor are modified into series connection [38]. C_i and R_i are calculated by using (8), (9), and (10), i.e., (4.7), (4.27), and (4.20) from [38] for the duty cycle $D = 0.5$.

$$\varnothing = atan\left[\frac{1 - Cos(2\pi D)}{2\pi(1 - D) + Sin(2\pi D)}\right] \tag{8}$$

$$\frac{C_i}{C_d} = \frac{\pi}{\left[\pi(1 - D) + Sin(2\pi D) - \frac{1}{4}Cos(2\varnothing)Sin(4\pi D) - \frac{1}{2}Sin(2\varnothing)Sin(2\pi D)^2 - 2\pi(1 - D)Sin(\varnothing)Sin(2\pi D - \varnothing)\right]} \tag{9}$$

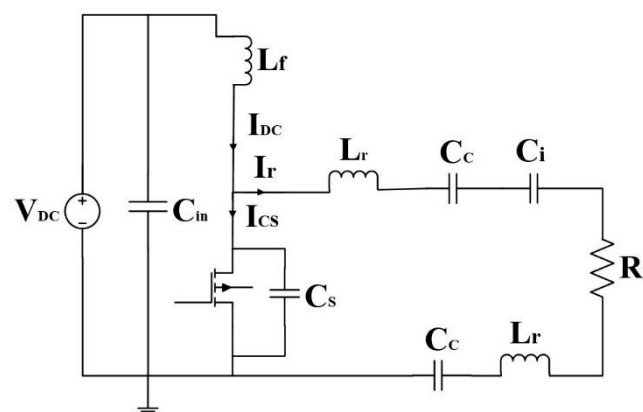$$\frac{R_i}{R_L} = 2Sin(\varnothing)^2 \tag{10}$$

Figure 4. Class-E^2 converter with equivalent rectifier circuit.

In the following section, the impedance equations are derived to find the optimal impedance point, and the variation in current through the choke inductor, switch, and resonant inductor is observed to identify the maximum power point.

3. Analysis on Optimal Impedance Tracking of Class-E^2 Converter

Class-E^2 converter is a simple circuit with fewer components. The impact of load variation is shown in [35]. It is also important to investigate the impact of different resonant inductors on the overall impedance of the circuit and the optimal impedance point is identified for each case. The analysis is performed by observing the impedance curves

for a range of frequencies. The impedance characteristics also determine the current flow through the choke inductor, MOSFET, and the primary resonant inductor for a range of frequencies. This method contributes to determining the Maximum power point. The output of the CPT system is dependent on the resonant network as it controls the power flow to the receiving section. As mentioned earlier, for this work the coupling plate pairs are placed far from each other, so mutual capacitance is ignored. From Figure 4 and Equation (11), the equivalent capacitance of the resonant network is the series combination of coupling plates and equivalent capacitor C_i. Resonant inductance on primary and secondary sections is considered equal resulting in a single resonant point. The work from [39] has examined two different values on primary and secondary inductors to realize multiple resonant points. Besides, the impedance of multi-resonant points will be larger than the single-resonant point, which limits the maximum current flow towards the rectifier section. Circuit parameters are listed in Table 1.

$$C_{eq} = \frac{2}{C_c} + \frac{1}{C_i} \tag{11}$$

$$Z_r = R_i + j \left[2 \times \omega L_r - \frac{1}{\omega C_{eq}} \right] \tag{12}$$

$$|Z_r| = \sqrt{R_i^2 + \left(2 \times \omega L_r - \frac{1}{\omega C_{eq}} \right)^2} \tag{13}$$

$$|Z_{in}| = R_{Lf} + \frac{|Z_r| \left| \frac{1}{\omega C_s} \right|}{|Z_r| + \left| \frac{1}{\omega C_s} \right|} \tag{14}$$

Table 1. Parameters of Class-E^2 power converter for CPT.

Parameters	Remark	Value
C_{in}	DC link/Input capacitor	100 nF
L_f	Choke inductor	18 µH
C_s	Shunt capacitor at switch	44 nF
C_c	Coupling capacitor	40 nF
L_r	Resonant inductor	18 µH/50 µH/100 µH
C_d	Shunt capacitor at diode	44 nF
L_s	Secondary inductor	18 µH
C_{out}	Output Capacitor	10 µF
R_L	Load resistance	2.2 Ω

The input impedance Z_{in} is derived in terms of resonant network and shunt capacitor presented in (14). The plots are presented considering the input voltage as 25 V for both theoretical and simulation analysis. As discussed earlier, the choke inductor (L_f) does not influence the resonant point for high inductance values. However, for low inductances, the choke inductor resonates with the shunt capacitor at the switch, resulting in the second resonant point. This is proved by performing hardware tests. However, from (14), the DC resistance/equivalent series resistance (ESR) of the choke inductor has an influence on overall input impedance. Different resonant inductors (L_r) are considered to investigate the impact of the resonant network on the input impedance Z_{in}. The remaining parameters of the Class-E^2 converter remain the same for each case. Using (14), the relation between the input impedance Z_{in} with respect to frequency is realized in Figure 5a. The impedance of the resonant network (Z_r) for different values of the inductor (i.e., L_r = 18 µH/50 µH/100 µH) can be tracked from Figure 5b. From Figure 5, the input impedance adjacent to the resonant point is measured to be the least, the frequency at which maximum power is transferred. It is defined as an optimal resonant point. For each case, i.e., for various resonant inductor (L_r) values, the optimal resonant point is observed in Figure 5a.
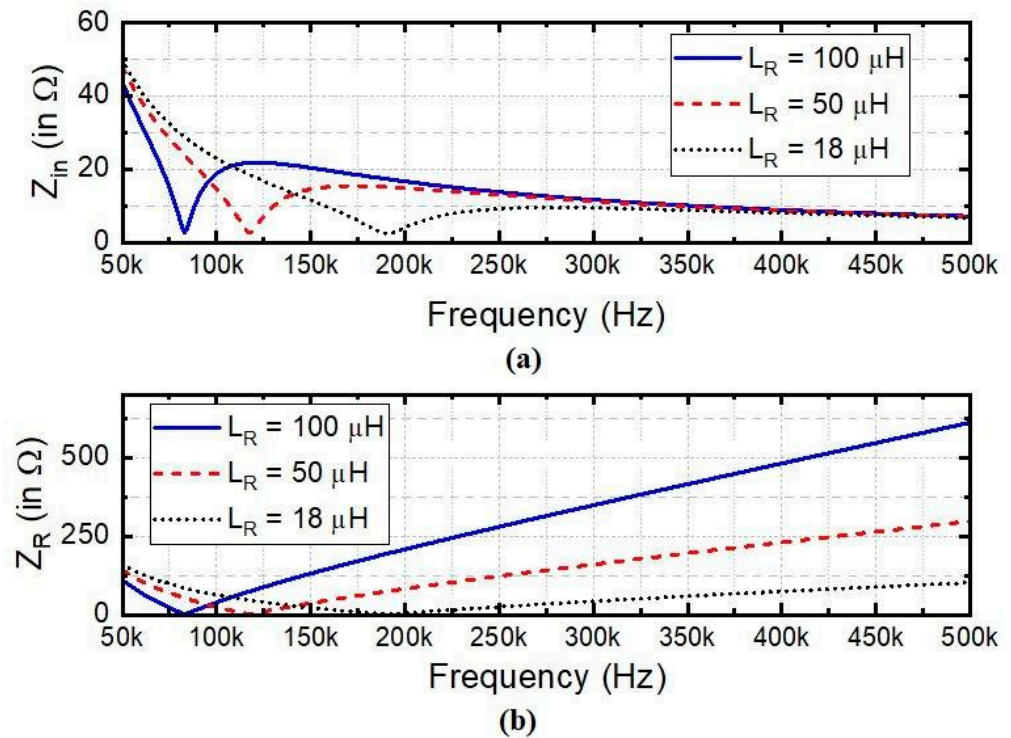
Figure 5. Impedance variation w.r.t frequency for different resonant inductance.

The theoretical results were compared with the simulation using an impedance analyzer from the Simulink. It is connected across the switch, and the input impedance is measured for all cases, i.e., L_r = 18 µH/50 µH/100 µH presented in Figure 6. Comparing Figures 5 and 6, the input impedance graph generated from Simulink closely matches the theoretical results. The optimal resonant point from the simulation matches the theoretical equations. It is important to mention that simulations are performed considering high secondary inductance (L_s = 1 mH), which minimizes the multi-resonant points. The input impedance and resonant network impedance drop significantly at the resonant frequency for each case. Additionally, the variation of phase angle with respect to the frequency shows whether input impedance is inductive or capacitive. The impedance increases w.r.t frequency when the phase angle is positive and decreases when the phase angle is negative; this leads to the circuit behavior being capacitive at a higher frequency. The impedance spike adjacent to the resonant frequency in Figure 6 is due to the diode and components at the receiving section.

$$I_{DC} = \frac{V_{DC}}{Z_{in}} \tag{15}$$

$$I_r = \frac{I_{DC} \times Z_r}{Z_r + Z_{C_s}} \tag{16}$$

$$I_{C_s} = I_{DC} - I_r \tag{17}$$

From Figure 7, input current (I_{DC}), switching current (I_{C_s}), and resonant current (I_r) can be tracked with respect to the frequency. The plot is realized for resonant inductor 50 µH. Clearly, at a resonant frequency, the input current (I_{DC}) is at maximum due to the low input impedance. The maximum current passed to the secondary section results in maximum power across the load. From the comparison of Z_{in} with I_{DC}, and Z_r with I_r, current curves are inverted versions of the impedance curves. As mentioned above, for frequencies over the resonant point, the input impedance drops significantly. But the resonant network's impedance increases as the operating frequency moves away from the resonant point resulting in low output power delivery. In this case, most of the current is passed to the switching section which is shown in Figure 7.
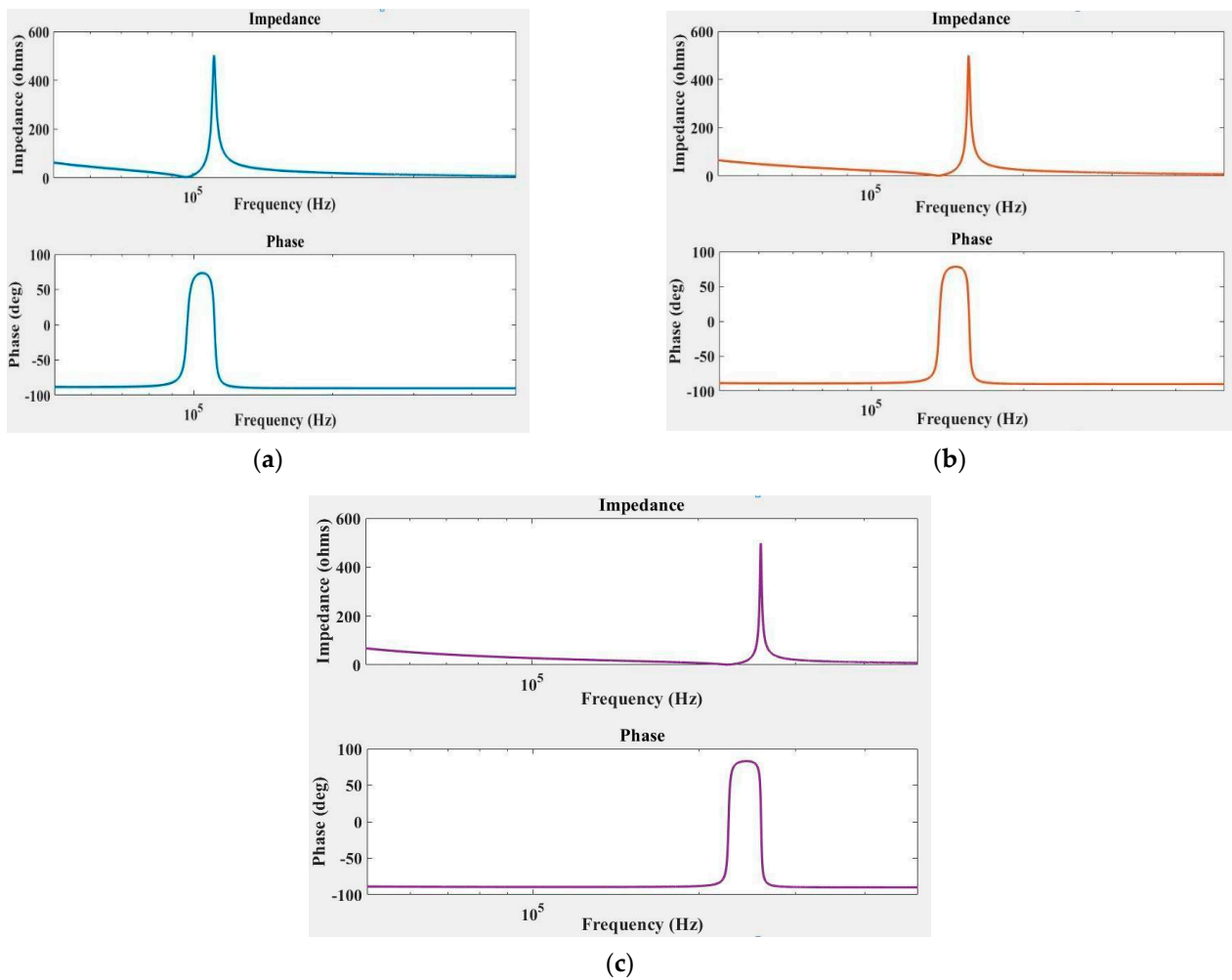
Figure 6. Simulink plots of input impedance w.r.t frequency (**a**) L_r = 100 μH, (**b**) L_r = 50 μH, and (**c**) L_r = 18 μH.
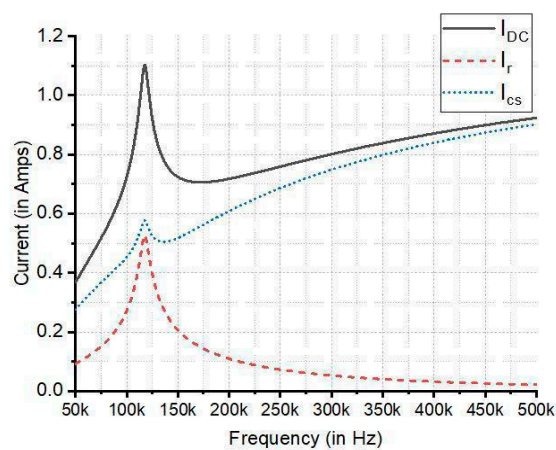

Figure 7. Variation of current through input side, MOSFET, and resonant network with respect to the frequency.

Similar to impedance, current curves are plotted for different resonant inductor values. Here, the input current (I_{DC1}), current through the resonant inductor (I_{r1}), and the current through a switch ($I_{C_s 1}$) are for L_r =100 μH. Similarly, I_{DC2}, I_{r2}, and $I_{C_s 2}$ are for L_r = 50 μH, and I_{DC3}, I_{r3}, and $I_{C_s 3}$ are for L_r = 18 μH. The amplitude of the current at a resonant point for each case can be seen in Figure 8a–c. With different resonant inductor values, the resonant

for each case can be seen in Figure 8a–c. With different resonant inductor values, the resonant point varies, and the amplitude of the current at the resonant point is also different for each case. It can be noted that, for the high resonant inductor value, the curve is much sharper compared to the CPT with a low resonant inductor value. In these cases, the impedance sensitivity is high for frequency variations resulting in significant changes in the load. For high frequencies, the switching current (I_{Cs}) curve remains almost the same for different resonant inductor values.
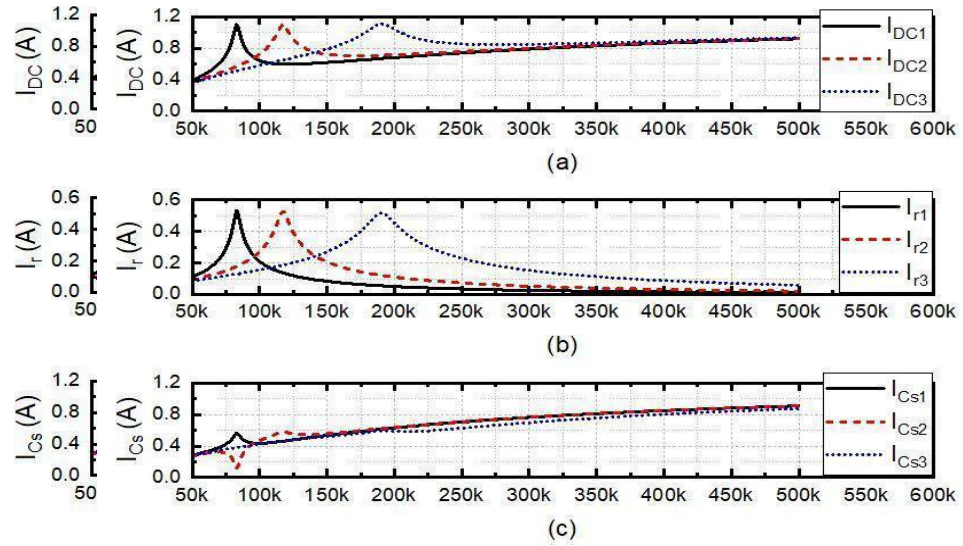

Figure 8. Variation of current through inverter side MOSFET, and resonant network for different resonant inductor values.

The prototype board of a Class-E² converter was designed, which can handle power up to 100 W. In Figure 9a, the Class-E inverter with a resonant inductor (L_r) can be seen, Figure 9b consists of a Class-E rectifier with the second resonant inductor (L_s), and Figure 9c shows the complete circuit with round capacitive coupling plates. To validate theoretical and simulation results, hardware tests were performed for 5 V input, and the input current and output voltage readings were noted down simultaneously. Here tests were performed for resonant inductors $L_r = 50$ µH and 100 µH, and 2.2 Ω load was connected at the output end.

Figure 9. *Cont.*
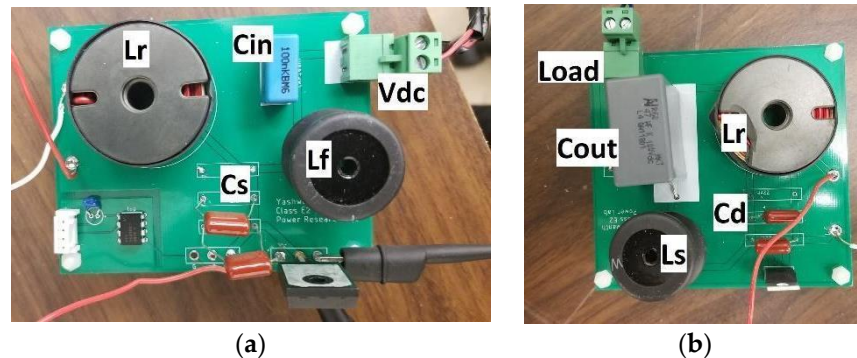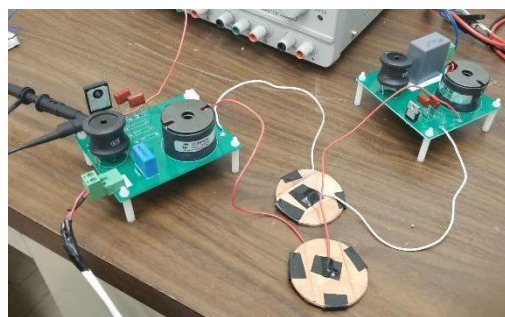
(**c**)

Figure 9. Hardware setup of the CPT system. (**a**) Class-E inverter. (**b**) Class-E rectifier. (**c**) Class-E2 converter with capacitive coupling plates.

Hardware tests were conducted for two cases i.e. $L_r = 50$ μH and $L_r = 100$ μH, and their respective resonant frequency points were defined as F_{R1} and F_{R2}. Figure 10 realize the input (I_{DC}) and output (V_{out}) voltage (V_{out}) of the hardware tests. Due to the nature of capacitive in the input circuit, the drop is significant for high frequencies and can be observed from Figure 10 that the input current increases with the wider operating frequencies, far from the resonant point. Even though output voltage is high at serval frequency points maximum efficiency (87%) is achieved only at the optimal impedance point, i.e. close to the resonant point. However, it is noticed that output voltage increases at a non-resonant frequency (F_{R11}) = 200 kHz for resonant in $L_r = 50$ μH. This occurs due to the low choke inductor (18 μH), which resonates with the shunt capacitor. Similarly, the output voltage increases slightly for $L_r = 100$ μH, at non-resonant frequency (F_{R22}) = 90 kHz. For high frequencies, the output voltage decreases gradually to zero due to high resonant impedance (Z_r). At low frequencies, the input impedance is expected to be inductive, leading to a high input current. When comparing both cases, the efficiency for $L_R = 50$ μH was found to be 87% at the optimal resonant point and 79% for $L_R = 100$ μH. Further to this, low resonant inductances could be considered but this would require the circuit to operate at a high operating frequency.
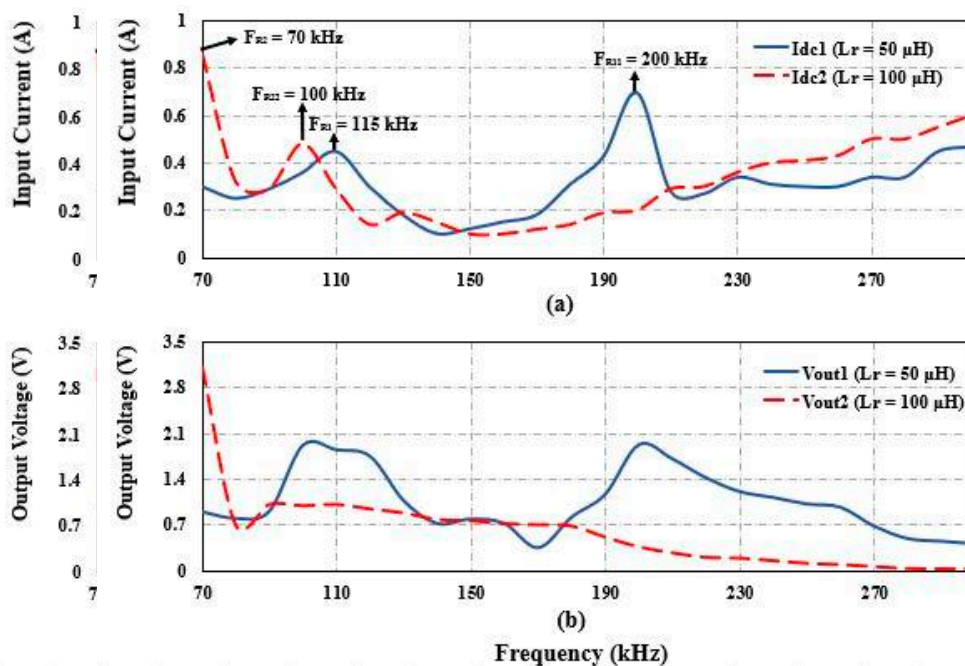
Figure 10. Hardware results of Class E² converter (**a**) Input current vs. Frequency, (**b**) Output Voltage vs. Frequency.

4. Discussion on the Impact of Duty and Frequency on ZVS Property

Along with the frequency, the variation of input current and output voltage was observed for different duty cycles. The relationship between the output voltage with respect to the duty cycle is majorly dependent on the shunt capacitor connected across the switch. As the Class-E converter has the ZVS configuration, it is important to identify the impact of change in frequency or duty cycle in order to maintain ZVS. The shunt capacitor affects the Class-E^2 converter in two ways: (1) The impedance that controls the current flow to the coupling plates, (2) ZVS configuration. Considering C_{Smax} is the maximum shunt capacitance to achieve ZVS, and C_S is the shunt capacitance. When $C_S < C_{Smax}$, the shunt capacitor voltage reaches zero, comparatively earlier to the closed switch as shown in Figure 11a. Figure 11b shows the plot when $C_S = C_{Smax}$. For both cases, below the resonant frequency (f_2 from (2)) the capacitor gets discharged, which leads to the flow of current to the ground. This results in low output voltage. For frequencies over f_1 (from (1)) the ZVS condition is lost, which also results in low output voltage as the operating frequency will be away from the resonant frequency. When it comes to the variation of a duty cycle for both cases, each one has different conditions. For $C_S < C_{Smax}$, the shunt capacitor starts discharging for the lower duty cycle (i.e., below 0.5). For duty cycle over 0.5, the output voltage remains constant until the ZVS condition is lost. The ZVS condition for the high duty cycle is dependent on the value of the shunt capacitor. For $C_S = C_{Smax}$, ZVS is lost for duty cycle over 0.5. For a low duty cycle, the output remains constant until the shunt capacitor starts discharging.
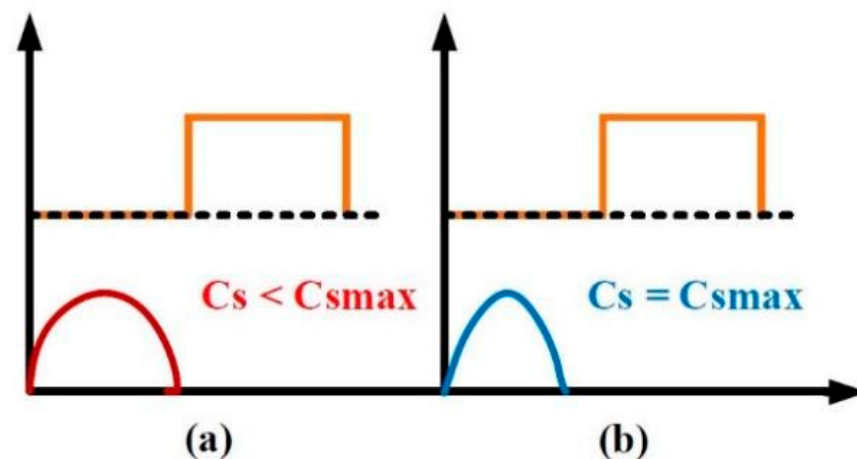
Figure 11. Waveform across the shunt capacitor (**a**) ZVS (**b**) early ZVS.

Hardware experiments were performed for duty cycle 0.3, 0.5, and 0.7 and frequency in a range [90–180 kHz]. The following readings are under the condition $C_S = C_{Smax}$, Figure 12 illustrates the voltage reading across shunt capacitor for various frequencies. From Figure 12c, for high frequencies with a duty cycle of 0.5, the ZVS condition is lost. ZVS is maintained for low frequencies until the shunt capacitor starts discharging as shown in Figure 12a. Figure 13 presents the voltage waveforms for the various duty cycles. From Figure 13a, when switching frequency 130 kHz for duty cycle 0.3 the capacitor discharges, which results in low output voltage. For a high duty cycle, the Class-E inverter loses its ZVS condition, shown in Figure 13c.

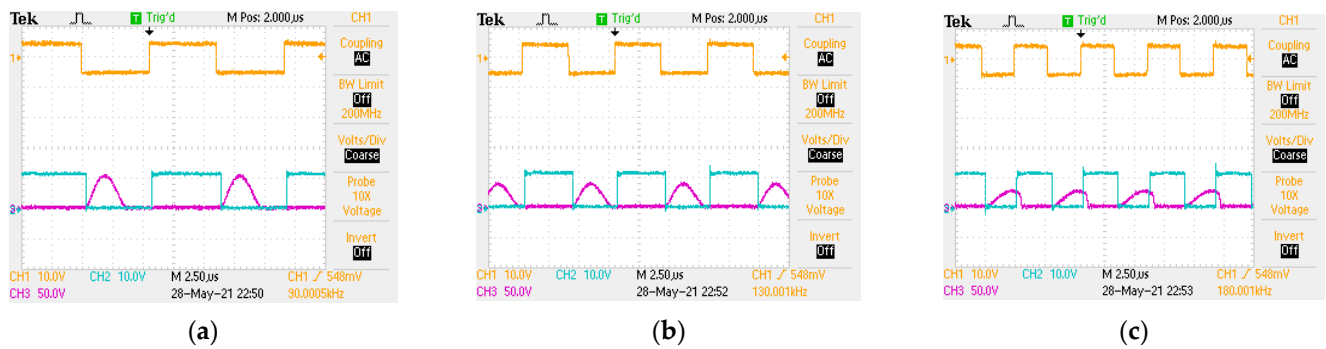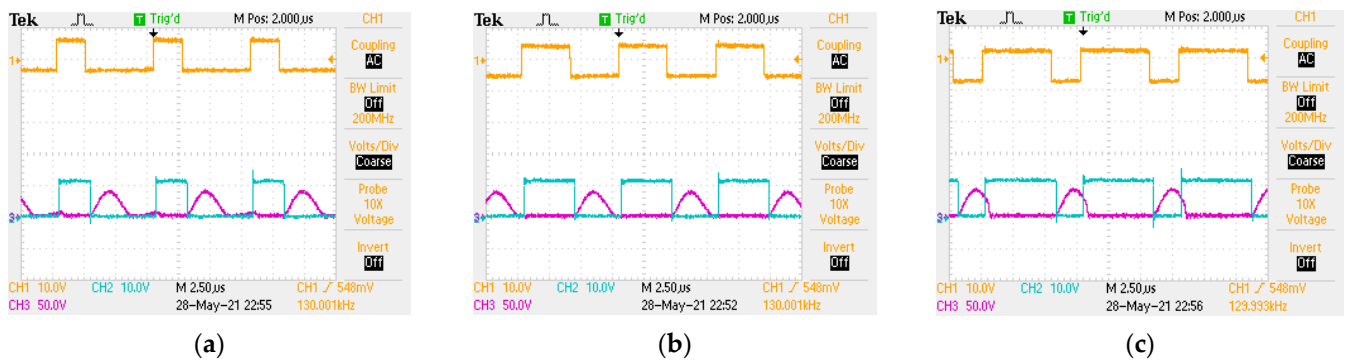**Figure 12.** Waveform across the shunt capacitor for frequency (**a**) 90 kHz, (**b**) 130 kHz, (**c**) 180 kHz.

Figure 13. Waveform across the shunt capacitor for duty cycle (**a**) *D* = 0.3, (**b**) *D* = 0.5, (**c**) *D* = 0.7.

The input impedance with respect to the duty cycle is presented by using Equations (12) and (17) [38]. With the increase in duty cycle from 0.5, the input impedance drops significantly resulting in a high current. Although it loses the ZVS condition, it does contribute to increasing the output voltage. This was proved by means of performing hardware experiments. Table 2 presents the input current, output voltage for various duty cycles, and frequencies. From Table 2, it can be observed that the output voltage is high when the switching frequency is close to resonant frequency, i.e., 100 kHz. But ZVS is achieved without discharging the shunt capacitor for operating frequencies over the resonant frequency. For switching frequency 130 kHz, the input current and output voltage can be noticed. The output voltage remains the same for duty cycle 0.3 and 0.5 and increases for 0.7. There is a 1% increase in output voltage for a 50% increase in input currents, which concludes with the drop in efficiency for a high duty cycle.

Table 2. Hardware results for various duty cycle and frequencies.

Frequency (kHz)	Input Current			Output Voltage		
	D = 0.3	*D* = 0.5	*D* = 0.7	*D* = 0.3	*D* = 0.5	*D* = 0.7
90	0.3	0.29	0.27	0.845	0.88	0.83
100	0.38	0.36	0.49	2.05	2.05	2.08
110	0.31	0.46	0.45	1.53	1.72	1.72
120	0.25	0.42	0.53	1.35	1.77	2.1
130	0.17	0.17	0.31	0.95	0.97	1.06
140	0.11	0.1	0.43	0.7	0.66	0.82
150	0.07	0.12	0.6	0.59	0.76	0.91

5. Conclusions

The impedance characteristics of the single-active switch is studied in this paper. Resonant inductor (L_r) and coupling plates are used as a compensation network for the

Class-E^2 power converter. Most previous works focus on the circuit behavior for load variation; this paper investigates the optimal impedance point for each resonant inductor. Theoretical equations and simulations conclude that the optimal impedance point is close to the resonant point. The reactance of the circuit at the optimal impedance point is relatively low resulting in high output voltage with maximum efficiency. Changes in the resonant inductor impact the amplitude of the input impedance, which is observed by means of impedance equations and proved by simulations. The prototype PCB board is developed to verify the theoretical and simulation results. Hardware tests are performed for 2.5 W; maximum efficiency of 87% is achieved at the optimal impedance point, i.e., close to resonant point F_{R1} = 100 kHz for L_r = 50 μH and 79% at 70 kHz for L_r = 100 μH. It can be noted that the choke inductor (L_f) resonates with the shunt capacitor for low inductances. To avoid such cases, the choke inductor with high inductance can be considered, the difference is observed from Figure 6. This paper also presents the variation of current at each component with respect to the frequency. It helps to track the maximum power point. Compared to previous works, this paper tracked the maximum efficiency point by means of impedance characteristics. Additionally, there is an increase of 9% in efficiency for L_r = 100 μH, and an increase of 17% for L_r = 50 μH, compared to prior studies in [35]. Besides, the ZVS property was analyzed for various duty cycles and frequencies. The limits of the ZVS can be observed for both frequency and duty cycle. From the results, it can be concluded that the output voltage increases with respect to the duty cycle but the maximum efficiency is achieved only by switching frequency 100 kHz for duty cycle 0.5 when $C_S = C_{S\max}$ (when L_r = 50 μH).

Author Contributions: Conceptualization, Y.B. and Y.Z.; methodology, Y.B.; software, Y.B.; validation, Y.B.; formal analysis, Y.B.; investigation, Y.B.; resources, Y.Z.; data curation, Y.B.; writing—original draft preparation, Y.B.; writing—review and editing, Y.B. and Y.Z.; visualization, Y.B.; supervision, Y.Z.; project administration, Y.Z.; funding acquisition, Y.Z. Both authors have read and agreed to the published version of the manuscript.

Conflicts of Interest: The authors declare no conflict of interest.

References

1. DeLong, B.J.; Kiourti, A.; Volakis, J.L. A radiating near-field patch rectenna for wireless power transfer to medical implants at 2.4 GHz. *IEEE J. Electromagn. RF Microw. Med. Biol.* **2018**, *2*, 64–69. [CrossRef]
2. Zhou, Y.; Liu, C.; Huang, Y. Wireless power transfer for implanted medical application: A review. *Energies* **2020**, *13*, 2837. [CrossRef]
3. Shaw, T.; Samanta, G.; Mitra, D. Efficient Wireless Power Transfer System for Implantable Medical Devices Using Circular Polarized Antennas. *IEEE Trans. Antennas Propag.* **2020**, in press. [CrossRef]
4. Sinha, S.; Kumar, A.; Regensburger, B.; Afridi, K.K. A new design approach to mitigating the effect of parasitics in capacitive wireless power transfer systems for electric vehicle charging. *IEEE Trans. Transp. Electrif.* **2019**, *5*, 1040–1059. [CrossRef]
5. Zhang, H.; Lu, F.; Hofmann, H.; Liu, W.; Mi, C.C. Six-plate capacitive coupler to reduce electric field emission in large air-gap capacitive power transfer. *IEEE Trans. Power Electron.* **2018**, *33*, 665–675. [CrossRef]
6. Subudhi, P.S.; Krithiga, S. Wireless power transfer topologies used for static and dynamic charging of EV battery: A review. *Int. J. Emerg. Electr. Power Syst.* **2020**. [CrossRef]
7. Sinha, S.; Kumar, A.; Regensburger, B.; Afridi, K.K. Active Variable Reactance Rectifier—A New Approach to Compensating for Coupling Variations in Wireless Power Transfer Systems. *IEEE J. Emerg. Sel. Top. Power Electron.* **2019**, *8*, 2022–2040. [CrossRef]
8. Park, C.; Park, J.; Shin, Y.; Kim, J.; Huh, S.; Kim, D.; Ahn, S. Separated Circular Capacitive Coupler for Reducing Cross-Coupling Capacitance in Drone Wireless Power Transfer System. *IEEE Trans. Microw. Theory Tech.* **2020**, *68*, 3978–3985. [CrossRef]
9. Raciti, A.; Rizzo, S.A.; Susinni, G. Drone charging stations over the buildings based on a wireless power transfer system. In Proceedings of the 2018 IEEE/IAS 54th Industrial and Commercial Power Systems Technical Conference (I&CPS), Niagara Falls, ON, Canada, 7–10 May 2018; pp. 1–6.
10. Aldhaher, S.; Mitcheson, P.D.; Arteaga, J.M.; Kkelis, G.; Yates, D.C. Light-Weight Wireless Power Transfer for Mid-Air Charging of Drones. In Proceedings of the 2017 11th European Conference on Antennas and Propagation (EUCAP), Paris, France, 19–24 March 2017; IEEE: Piscataway, NJ, USA, 2017; pp. 336–340.

11. Tampubolon, M.; Pamungkas, L.; Chiu, H.J.; Liu, Y.C.; Hsieh, Y.C. Dynamic wireless power transfer for logistic robots. *Energies* **2018**, *11*, 527. [CrossRef]

12. Sakhdari, M.; Hajizadegan, M.; Chen, P.Y. Robust extended-range wireless power transfer using a higher-order PT-symmetric platform. *Phys. Rev. Res.* **2020**, *2*, 013152. [CrossRef]

13. Le, A.M.; Truong, L.H.; Quyen, T.V.; Nguyen, C.V.; Nguyen, M.T. Wireless power transfer near-field technologies for unmanned aerial vehicles (uavs): A review. *EAI Endorsed Trans. Ind. Netw. Intell. Syst.* **2020**, *7*, 162831. [CrossRef]

14. Sedwick, R.J. Long range inductive power transfer with superconducting oscillators. *Ann. Phys.* **2020**, *325*, 287–299. [CrossRef]

15. Choi, B.H.; Lee, E.S.; Kim, J.H.; Rim, C.T. 7m-Off-Long-Distance Extremely Loosely Coupled Inductive Power Transfer Systems Using Dipole Coils. In Proceedings of the 2014 IEEE Energy Conversion Congress and Exposition (ECCE), Pittsburgh, PA, USA, 14–18 September 2014; IEEE: Piscataway, NJ, USA, 2014; pp. 858–863.

16. Liu, C.; Hu, A.P. *Wireless/Contactless Power Transfer: Capacitively Coupled Solutions*; LAP Lambert Academic Publishing: Chisinau, Moldova, 2012.

17. Lu, F.; Zhang, H.; Mi, C. A review on the recent development of capacitive wireless power transfer technology. *Energies* **2017**, *10*, 1752. [CrossRef]

18. Lu, F.; Zhang, H.; Mi, C. A two-plate capacitive wireless power transfer system for electric vehicle charging applications. *IEEE Trans. Power Electron.* **2017**, *33*, 964–969. [CrossRef]

19. Dai, J.; Ludois, D.C. Capacitive power transfer through a conformal bumper for electric vehicle charging. *IEEE J. Emerg. Sel. Top. Power Electron.* **2015**, *4*, 1015–1025. [CrossRef]

20. Yi, K. Capacitive coupling wireless power transfer with quasi-llc resonant converter using electric vehicles' windows. *Electronics* **2020**, *9*, 676. [CrossRef]

21. Domingos, F.C.; de Freitas, S.V.D.C.; Mousavi, P. Capacitive Power Transfer based on Compensation Circuit for Class E Resonant Full-Wave Rectifier. In Proceedings of the 2018 IEEE Wireless Power Transfer Conference (WPTC), Montreal, QC, Canada, 3–7 June 2018; IEEE: Piscataway, NJ, USA, 2018; pp. 1–4.

22. Mostafa, T.M.; Muharam, A.; Hattori, R. Wireless Battery Charging System for Drones VIA capacitive Power Transfer. In Proceedings of the 2017 IEEE PELS Workshop on Emerging Technologies: Wireless Power Transfer (WoW), Chongqing, China, 20–22 May 2017; IEEE: Piscataway, NJ, USA, 2017; pp. 1–6.

23. Liang, H.R.; Lee, C.K.; Hui, S.R. Design, Analysis, and Experimental Verification of a Ball-Joint Structure With Constant Coupling for Capacitive Wireless Power Transfer. *IEEE J. Emerg. Sel. Top. Power Electron.* **2019**, *8*, 3582–3591. [CrossRef]

24. da Silva, G.G.; Petry, C.A. Capacitive Wireless Power Transfer System Applied to Low-Power Mobile Device Charging. *Int. J. Electr. Energy* **2015**, *3*, 230–234. [CrossRef]

25. Choi, J.; Tsukiyama, D.; Tsuruda, Y.; Davila, J.M.R. High-frequency, high-power resonant inverter with eGaN FET for wireless power transfer. *IEEE Trans. Power Electron.* **2017**, *33*, 1890–1896. [CrossRef]

26. Regensburger, B.; Kumar, A.; Sinha, S.; Doubleday, K.; Pervaiz, S.; Popovic, Z.; Afridi, K. High-performance large air-gap capacitive wireless power transfer system for electric vehicle charging. In Proceedings of the 2017 IEEE Transportation Electrification Conference and Expo (ITEC), Chicago, IL, USA, 22–24 June 2017; pp. 638–643.

27. Huang, L.; Hu, A.P.; Swain, A. A resonant compensation method for improving the performance of capacitively coupled power transfer system. In Proceedings of the 2014 IEEE Energy Conversion Congress and Exposition (ECCE), Pittsburgh, PA, USA, 14–18 September 2014; IEEE: Piscataway, NJ, USA, 2014; pp. 870–875.

28. Wang, N.X.; Wang, H.W.; Mei, J.; Mohammadi, S.; Moon, J.; Lang, J.H.; Kirtley, J.L. Robust Wireless Power Transfer System Based on Rotating Fields for Multi-User Charging. *IEEE Trans. Energy Convers.* **2021**, *36*, 693–702. [CrossRef]

29. Narayanamoorthi, R.; Vimala Juliet, A.; Chokkalingam, B.; Padmanaban, S.; Leonowicz, Z.M. Class E power amplifier design and optimization for the capacitive coupled wireless power transfer system in biomedical implants. *Energies* **2017**, *10*, 1409.

30. Dai, J.; Hagen, S.; Ludois, D.C.; Brown, I.P. Synchronous generator brushless field excitation and voltage regulation via capacitive coupling through journal bearings. *IEEE Trans. Ind. Appl.* **2017**, *53*, 3317–3326. [CrossRef]

31. Li, S.; Liu, Z.; Zhao, H.; Zhu, L.; Shuai, C.; Chen, Z. Wireless power transfer by electric field resonance and its application in dynamic charging. *IEEE Trans. Ind. Electron.* **2016**, *63*, 6602–6612. [CrossRef]

32. Qing, X.D.; Wang, Z.H.; Su, Y.G.; Zhao, Y.M.; Wu, X.Y. Parameter Design Method with Constant Output Voltage Characteristic for Bilateral LC-Compensated CPT System. *IEEE J. Emerg. Sel. Top. Power Electron.* **2019**, *8*, 2707–2715. [CrossRef]

33. Wu, Y.; Chen, Q.; Ren, X.; Zhang, Z. Efficiency Optimization Based Parameter Design Method for the Capacitive Power Transfer System. *IEEE Trans. Power Electron.* **2021**, *36*, 8774–8785. [CrossRef]

34. Lu, F.; Zhang, H.; Hofmann, H.; Mi, C.C. A double-sided LC-compensation circuit for loosely coupled capacitive power transfer. *IEEE Trans. Power Electron.* **2017**, *33*, 1633–1643. [CrossRef]

35. Mostafa, T.M.; Bui, D.; Muharam, A.; Hu, A.P.; Hattori, R. Load effect analysis and maximum power transfer tracking of CPT system. *IEEE Trans. Circuits Syst. I Regul. Pap.* **2020**, *67*, 2836–2848. [CrossRef]

36. Dai, J.; Ludois, D.C. Single active switch power electronics for kilowatt scale capacitive power transfer. *IEEE J. Emerg. Sel. Top. Power Electron.* **2014**, *3*, 315–323.

37. Bezawada, Y.; Fu, R.; Zhang, Y. Impacts of Coupling Plates on Single-Switch Capacitive-Coupled WPT Systems. In Proceedings of the 2019 IEEE PELS Workshop on Emerging Technologies: Wireless Power Transfer (WoW), London, UK, 18–21 June 2019; IEEE: Piscataway, NJ, USA, 2019; pp. 330–334.

38. Kazimierczuk, M.K.; Czarkowski, D. *Resonant Power Converters*; John Wiley & Sons: Hoboken, NJ, USA, 2012.
39. Bezawada, Y.; Fu, R.; Zhang, Y. Analyzing Resonant Points of SLLD Circuit to Achieve MPPT for Capacitive-Coupling Wireless Power Transfer. In Proceedings of the 2019 IEEE Energy Conversion Congress and Exposition (ECCE), Baltimore, MD, USA, 29 September–3 October 2019; IEEE: Piscataway, NJ, USA, 2019; pp. 3353–3357.
40. Pamungkas, L.; Wu, S.H.; Chiu, H.J. Equivalent Circuit Approach for Output Characteristic Design of Capacitive Power Transfer. *IEEE Trans. Circuits Syst. II Express Briefs* **2021**, in press.
41. Xia, H.; Wu, H.; Cheng, Y.; Wang, G. A Design Procedure for CPT System with LCL Resonant Network. In Proceedings of the 2019 IEEE Wireless Power Transfer Conference (WPTC), London, UK, 18–21 June 2019; IEEE: Piscataway, NJ, USA, 2019; pp. 76–79.